water

MDPI

Article

The Displacement of the Resident Wetting Fluid by the Invading Wetting Fluid in Porous Media Using Direct Numerical Simulation

Yung-Li Wang [1,2], Qun-Zhan Huang [1] and Shao-Yiu Hsu [1,*]

[1] Department of Bioenvironmental Systems Engineering, National Taiwan University, Taipei 10617, Taiwan; d06622003@ntu.edu.tw (Y.-L.W.); d09622003@ntu.edu.tw (Q.-Z.H.)
[2] Green Energy and Environment Research Laboratories, Industrial Technology Research Institute, Hsinchu 31057, Taiwan
* Correspondence: syhsu@ntu.edu.tw; Tel.: +886-2-3366-4671

Abstract: Understanding the displacement of the resident wetting fluid in porous media is crucial to the remediation strategy. When pollutants or nutrients are dissolved in the surface wetting fluid and enter the unsaturated zone, the resident wetting fluid in the porous system may remain or be easily flushed out and finally arrive in the groundwater. The fate and transport of the resident wetting fluid determine the policy priorities on soil or groundwater. In this study, the displacement of the resident wetting fluid by the invading wetting fluid in porous media was simulated using direct numerical simulation (DNS). Based on the simulations of the displacements in porous media, the effect of the non-wetting fluid on the displacement was evaluated by observation and quantification, which were difficult to achieve in laboratory experiments. The result can also explain the unknown phenomenon in previous column experiments, namely that the old water is continuously released from the unsaturated porous media even after a long period of flushing with the new water. The effects of the interfacial tension, contact angle, and injection rate, which affected the immiscible fluid–fluid flow pattern, were also evaluated. Since pollutants dissolved in the wetting fluid could change the physical properties of the wetting fluid, the interfacial tensions of the resident wetting fluid and the invading wetting fluid were set separately in the simulation. Moreover, our simulation demonstrated that the consecutive drainage–imbibition cycles could improve the displacement of the resident wetting fluid in porous media. The successful simulation in this study implied that this method can be applied to predict other immiscible fluid–fluid flow in natural or industrial processes.

Keywords: wetting fluid; non-wetting fluid; porous media; direct numerical simulation (DNS)

check for updates

Citation: Wang, Y.-L.; Huang, Q.-Z.; Hsu, S.-Y. The Displacement of the Resident Wetting Fluid by the Invading Wetting Fluid in Porous Media Using Direct Numerical Simulation. *Water* **2023**, *15*, 2636. https://doi.org/10.3390/w15142636

Academic Editors: Qinzhuo Liao, Sanbai Li and Shihao Wang

Received: 16 June 2023
Revised: 15 July 2023
Accepted: 17 July 2023
Published: 20 July 2023

Copyright: © 2023 by the authors. Licensee MDPI, Basel, Switzerland. This article is an open access article distributed under the terms and conditions of the Creative Commons Attribution (CC BY) license (https://creativecommons.org/licenses/by/4.0/).

1. Introduction

Multiphase flow in porous media plays a key role in natural or industrial processes, including transporting pollutants or nutrients in soils, geologic carbon sequestration, groundwater remediation, and enhanced oil recovery [1–4]. The vadose zone, or so-called unsaturated zone, is the interface connecting land surface and groundwater. When pollutants or nutrients released from the surface enter the vadose zone, they may remain in the vadose zone or be flushed out by the following invading water and enter the groundwater. Whether the pollutants or nutrients stay in the vadose zone or finally enter groundwater determines the government's pollution remediation strategy on soil or groundwater. Therefore, understanding the displacement efficiency of the resident wetting fluid in porous media by the following invading wetting fluid helps decide the policy priorities. For example, in the porous system, the transport and retention behaviors of per- and poly-fluoroalkyl substances (so-called "PFAS"), a family of persistent organic pollutants [5], are widely investigated [6–9].

The displacement efficiency of the resident wetting fluid in porous media is influenced by many factors, including pore geometry, the presence of the non-wetting fluid, interfacial tension, the contact angle, the injection rate, and consecutive drainage and imbibition cycles. These factors cause uncertainty in estimating the fate of pollutants.

"Trapped air" (the non-wetting fluid) has been proven to affect the flow pattern of the wetting fluid in porous media during infiltration [10,11]. Understanding the interplay between "old water" (the resident wetting fluid) and "new water" (the invading wetting fluid) in porous media with "air" (the non-wetting fluid) helps evaluate the displacement efficiency of old water. Gouet-Kaplan and Berkowitz (2011) [12] used a 2D glass micromodel and image analysis to observe the dynamics of old-new water exchange. Gouet-Kaplan et al. (2012) [13] used conservative tracers to monitor the solute transport in column experiments. Although the experiments mentioned above [12,13] were carried out under partially saturated conditions, the effect of "air" on the old-new water interplay was not fully discussed. How the old water was trapped in the system and why the old water was unceasingly monitored in the outflow even over a long-time scale [13] were never elucidated.

Interfacial tension is the adhesive force between two substances. The displacement efficiency of the resident wetting fluid in porous media will vary with surface tension (the interfacial tension of the "air–water" interface) because this property affects the flow behavior of fluids. In a natural system, pollutants or nutrients dissolved in water can change the surface tension of the solution. For example, inorganic salts, such as NaCl and $CaCl_2$, would increase the surface tension [14], while some miscible pollutants, such as amines, alcohols, and other organic compounds, would reduce the surface tension of water [15].

Wettability is the ability of a liquid to adhere to a solid surface, and different porous materials have different wettability. The wettability can be expressed by measuring the contact angle between the liquid and the solid. A contact angle greater than 90° indicates a hydrophobic surface, while a contact angle less than 90° indicates a hydrophilic surface. Decreasing the contact angle increases the capillary pressure, the pressure difference across the interface between two immiscible fluids in porous media, which means that the wetting fluid will displace more of the non-wetting fluid. Therefore, the flow pattern and distribution of the resident wetting fluid in porous media will change with the contact angle.

The injection rate of the invading wetting fluid influences the displacement efficiency of the resident wetting fluid in porous media. Theoretically, a higher injection rate of the invading wetting fluid has a stronger driving force to flush out the resident wetting fluid as well as the non-wetting fluid in porous media. However, a higher injection rate may result in preferential flow in porous media so that the invading wetting fluid flows out quickly through the preferential pathway and has less opportunity to mix with the resident wetting fluid in porous media and displace it. Thus, not simply the injection rate, but whether the resident wetting fluid can mix with the invading wetting fluid is what completely determines the displacement efficiency.

"Imbibition" means increasing the saturation of the wetting fluid and decreasing the saturation of the non-wetting fluid, while "drainage" means decreasing the saturation of the wetting fluid and increasing the saturation of the non-wetting fluid. The cycle of imbibition and drainage occurs repetitively in the nature system's unsaturated zone. Li et al. (2013) [16] conducted a series of column experiments to study the saturation–capillary pressure relation under consecutive drainage–imbibition cycles. During consecutive imbibition–drainage cycles, the saturation of the non-wetting phase (S_{nw}) varied in the stable and unstable states. The results revealed that the stability of trapped air in the porous medium was affected by the consecutive drainage–imbibition cycles. Tavangarrad et al. (2019) [17] evaluated the effect of multiple imbibition–drainage cycles on capillary pressure–saturation curves of thin hydrophilic fibrous layers. The result showed that if a sample was wetted in the first imbibition–drainage cycle, the capillary phenomenon would be more obvious in the

next cycles. The discussion mentioned above infers that the drainage–imbibition cycles influence the two immiscible fluid–fluid flows in porous media and the displacement of the resident wetting fluid.

Several laboratory methods, such as the 2D glass micromodel [12] and the Dacry-scale column experiment [13], have been developed to study the displacement and mixing of the resident wetting fluid by the invading wetting fluid in porous media. For instance, Gouet-Kaplan and Berkowitz (2011) [12] applied dyes in the 2D glass micromodel to observe the interplay between old water and new water. Although the saturations of water can be quantified by volumetric fractions, the concentrations of water, especially the partially mixing zone, cannot be accurately quantified.

Visualizing and quantifying the interplay between the resident wetting fluid and the invading wetting fluid in porous media are useful to study the displacement efficiency of the resident wetting fluid and to evaluate related influencing factors. However, measuring the local concentration of the solute in porous media is always challenging. Although techniques based on Beer's Law have been developed and applied to column experiments [18,19], these measurements of local concentrations are the average values over several pore sizes. They cannot meet the detection requirements for pore-scale research. Only a few experimental methods using the fluorescent tracer can precisely measure the local concentration in pores [20]. However, fluorescence analysis requires advanced skills and is not yet widely applied to pore-scale research.

Unlike traditional laboratory experiments, the computational method is a useful tool to simulate the multiphase flow in porous media for investigating the displacement efficiency of the resident wetting fluid. The simulation can provide quantified information that is difficult to measure or completely acquire in laboratory experiments. With recent advances in computational resources, several approaches, including smoothed particle hydrodynamics (SPH) [21–23], the lattice Boltzmann method (LBM) [24–26], and direct numerical simulation (DNS) [27,28], have been developed to simulate the multiphase flows in pore-scale systems.

Smoothed particle hydrodynamics (SPH) is a mesh-free Lagrangian method [21,28]. SPH regards a continuous fluid as an interacting particle group that carries various physical quantities. By solving the particle group's dynamic equation and recording the movement of each particle, the mechanical behavior of the whole system will be obtained. The Lattice Boltzmann method (LBM), which is intrinsically a mesoscopic method to simulate fluid flows, is considered an alternative to traditional computational fluid dynamics (CFD) [28]. Unlike traditional CFD that solves macroscopic conservative equations (Navier–Stokes equations), the fluid in LBM is regarded as a discrete system composed of large numbers of particles. The behavior of these particles is described based on mesoscopic kinetic equations and then is converted to the macroscopic properties of the fluids.

In contrast to the SPH or LBM methods, direct numerical simulation (DNS) straightforwardly solves Navier–Stokes equations to obtain the instantaneous fluid physical quantities at a specific time position. DNS coupling with interface tracking and capturing approaches can truly simulate high density and high viscosity ratios of two immiscible fluids in porous media, which is always challenging in simulations [27,29]. Since the DNS method is based on conservation principles, and the simulations faithfully describe the two-phase flow and successfully capture the deformation of the fluid–fluid interface in porous media, we applied DNS coupled with the VOF method, whose model parameters were physical properties of the fluids, for the following research.

The aim of this study was to provide simulation-based evidence that supports and validates previous experimental observations. Additionally, the study sought to elucidate the potential mechanism by which the non-wetting fluid affected the separation of the resident and invading wetting fluid. With DNS, the displacements of the resident wetting fluid (w_1) by the invading wetting fluid (w_2) in porous media under different conditions were simulated. The effects of the non-wetting fluid (nw), interfacial tension (σ_{w1nw}), contact angle (θ), injection rate, and drainage–imbibition cycles on the displacements

were evaluated by observing and quantifying the simulation results. Furthermore, the implications and significance of these simulation results for research and applications in the environmental field were discussed in the following sections.

2. Methodology

All CFD simulations in this study were performed using the finite volume method via OpenFOAM software (OpenFOAM v9) [30]. The workflow diagram of OpenFOAM was referred to as Figure A1 (Appendix A). The Navier–Stokes equations were solved by direct numerical simulation (DNS). The volume of fluid (VOF) method [31] was applied to capture the immiscible fluid–fluid interface.

2.1. Navier-Stokes Equations

The two-phase flow system studied in this article was assumed to be isothermal. Both the wetting phase and the non-wetting phase were considered incompressible. Therefore, the two-phase flow was governed by Navier–Stokes equations, of which the continuity equation (Equation (1)) and momentum equation (Equation (2)) were:

$$\nabla \cdot u = 0 \tag{1}$$

and

$$\frac{\partial \rho \mu}{\partial t} + \nabla \cdot (\rho u u) = -\nabla p + \nabla \cdot \left[\mu \left(\nabla u + \nabla u^T \right) \right] + F_s \tag{2}$$

where u, ρ, μ, p, and F_s denoted velocity, density, viscosity, pressure, and surface force, respectively.

2.2. Volume of Fluid (VOF) Method

The VOF method was a surface-tracking approach in CFD for tracking the motion of an immiscible fluid–fluid interface applied in Eulerian mesh [31]. In a two-phase flow system, each phase was represented by its volume fraction α (α = 1 referred to as fully occupied by the wetting phase, while α = 0 referred to as fully occupied by the non-wetting phase), and the interface grid cells were represented by the intermediate values of α ($0 < \alpha < 1$). Moreover, the density (ρ) and viscosity (μ) varied in space and time were expressed as follows:

$$\begin{cases} \rho = \alpha \rho_w + (1 - \alpha) \rho_{nw} \\ \mu = \alpha \mu_w + (1 - \alpha) \mu_{nw} \end{cases} \tag{3}$$

where the subscripts "w" denoted the wetting phase and "nw" denoted the non-wetting phase. The volume fraction α was obtained by solving a simple advection equation (Equation (4)) as follows:

$$\frac{\partial \alpha}{\partial t} + \nabla \cdot (\alpha u) + \nabla \cdot (\alpha (1 - \alpha) u_r) = 0 \tag{4}$$

where u_r was the relative velocity between two phases.

Additionally, the surface force (F_s) imposed on the interface and changing with volume fraction was expressed as $F_s = \sigma k \nabla \alpha$, where σ is the interfacial tension and k is the curvature of the interface. The curvature of the interface k, defined as the divergence of a unit normal vector $\hat{n}$, was expressed as $\kappa = -\nabla \cdot \hat{n} = -\nabla \cdot \left(\frac{\nabla \alpha}{\|\nabla \alpha\|} \right)$. The wettability was expressed by the static contact angle (θ) following the equation $\hat{n} = \hat{n}_w cos\theta + \hat{t}_w cos\theta$, where $\hat{n}_w$ and $\hat{t}_w$ were the unit normal vector to the solid and the unit tangent vector to the solid, respectively [28,32,33].

In this study, OpenFOAM's solver interMixingFoam, which was developed for 3 incompressible fluids of which 2 were miscible, was selected to implement the computation. The interMixingFoam solver was developed based on the interFoam solver (for 2 incompressible and immiscible fluids). The performance of the interFoam solver using the VOF approach based on OpenFOAM was evaluated by Deshpande et al. in 2012 [34],

and the result indicated that the algorithm of the solver ensured a consistent formulation of pressure and interfacial tension. As for the mixing of the two miscible fluids, the resident wetting fluid (w_1) and the invading wetting fluid (w_2), the process was regarded as a solute transport phenomenon and described as the following advection–diffusion equation:

$$\frac{\partial C}{\partial t} + u \cdot \nabla C - \nabla \cdot (D_m \nabla C) = 0 \quad (5)$$

where C is the concentration of w_1 (or w_2) and D_m is the diffusivity.

2.3. Numerical Domain, Boundary, and Initial Conditions

All the numerical domains were two-dimensional (2D) square geometries (7.5 mm × 7.5 mm) containing N cylindrical grains (solid obstacles) with radii of R. Six micromodels (Appendix A Figure A2 were used in this study. Micromodel 1, Micromodel 2, and Micromodel 3 had the same grain size and porosity, but they were different in the spatial distribution of the grain. Micromodel 4 and Micromodel 5 had similar porosity to Micromodel 1 (Micromodel 2, Micromodel 3), but had different grain sizes and pore throats, which would result in different capillary pressure. Micromodel 6 had the same grain size as Micromodel 1 (Micromodel 2, Micromodel 3), but had larger porosity. The porosities of Micromodel 1 (the same as Micromodel 2 and Micromodel 3), Micromodel 4, Micromodel 5, and Micromodel 6 were 49.73% (N = 36, R = 5×10^{-4} m), 48.39% (N = 64, R = 3.8×10^{-4} m), 49.73% (N = 25, R = 6×10^{-4} m), and 65.09% (N = 25, R = 5×10^{-4} m), respectively.

All the domains were meshed by OpenFOAM's mesh generators, blockMesh and snappyHexMesh. The mesh generation process was described as follows: (1) The blockMesh generated structured hexahedral meshes as the background mesh; (2) the snappyHexMesh generated high-quality hexahedral and split-hexahedral meshes near the surface of the geometry. To ensure the accuracy of the simulations while saving computational resources, the mesh discretization in this study was based on the evaluation results of Ferrari and Lunati (2013) [27]. Ferrari and Lunati (2013) [27] used DNS coupled with the VOF method via OpenFOAM to simulate the immiscible fluid–fluid flow in a porous system similar to the pore structures adopted in this study (a 2D domain containing cylindrical obstacles). Five different discretization levels, defined by $d/\Delta x$ (where d represents the mean pore diameter and Δx represents the typical cell size), including $d/\Delta x$ = 8, 12, 15, 24, and 48, were tested to assess the effect of discretization on the simulation. The result showed that the difference between $d/\Delta x$ = 8 and the finest mesh $d/\Delta x$ = 48) was approximately 15%, while the relative errors of the others ($d/\Delta x$ = 12, 15, 24) were all within 10%. In this study, $d/\Delta x \approx 12$ was selected to construct the mesh. The total number of mesh cells for Micromodel 1, Micromodel 2, Micromodel 3, Micromodel 4, Micromodel 5, and Micromodel 6 were 38,780, 38,673, 38,769, 48,284, 33,877, and 33,371, respectively.

The left boundary was set up as an inlet with constant velocity and the right boundary was set up as an outlet with constant pressure zero. The solid phase, including top and bottom boundaries, and solid obstacles, were set up as "no-slip" conditions. In this study, a series of simulations of the displacement of w_1 by w_2 in porous media with or without nw were implemented. All the properties for simulations are listed in Table 1.

To evaluate the effect of the non-wetting phase (Section 3.1), Micromodel 1 under different conditions, with and without nw, was simulated for comparison. Initially, the system was assumed to be filled with w_1. As for the condition without nw, w_2 was directly injected into the system at a constant rate (0.05 m/s). As for the condition with nw, nw was first injected into the system at a constant rate (0.05 m/s). After dynamic balance, w_2 was injected into the system at a constant rate (0.05 m/s), and monitoring of the displacement started.

To evaluate the effects of interfacial tension (σ_{w1nw}) and contact angle (θ) (Section 3.2), three micromodels (Micromodel 1, Micromodel 2, and Micromodel 3) with little difference in the spatial distribution of the grain were adopted to avoid an extremely abnormal result causing misinterpretation. All the simulations were assumed under the condition with nw.

At first, *nw* was injected into the system, which was assumed to be initially filled with w_1, at a constant rate (0.05 m/s). After dynamic balance, w_2 was injected into the system at a constant rate (0.05 m/s), and monitoring of the displacement started. During the injection process of *nw*, all the parameters for simulation were the same as in Table 1 to ensure that the initial conditions for all cases were identical. When w_2 started entering the system, the parameters, interfacial tension (σ_{w1nw}), or contact angle (θ) were changed for comparison.

Table 1. Properties of the fluids used in the simulations.

Parameter	Value	Unit
density, ρ_{w1}	1000	kg/m^3
density, ρ_{w2}	1000	kg/m^3
density, ρ_{nw}	1	kg/m^3
kinetic viscosity, ν_{w1}	10^{-6}	m^2/s
kinetic viscosity, ν_{w2}	10^{-6}	m^2/s
kinetic viscosity, ν_{nw}	1.48×10^{-5}	m^2/s
interfacial tension, σ_{w1nw}	0.0707	kg/s^2
interfacial tension, σ_{w2nw}	0.0707	kg/s^2
Diffusivity, D_{w1w2}	3×10^{-9}	-
contact angle, θ	45	$^\circ$ (degree)

To evaluate the effect of the injection rate (Section 3.3), Micromodel 2 was simulated at different injection rates of w_2 for comparison under the condition with *nw*. At first, *nw* was injected into the system, which was assumed to be initially filled with w_1, at a constant rate (0.05 m/s). After dynamic balance, w_2 was injected into the system at a constant rate and monitoring of the displacement started. As for the high injection rate condition, the rate was 0.05 m/s for 0.2 s, while for the low injection rate condition, the rate was 0.01 m/s for 1 s.

To evaluate the effect of drainage–wetting cycles (Section 3.4), the micromodels (Micromodel 1~Micromodel 6) were simulated by injecting two cycles of *nw* followed by w_2 into the system. Initially, the system was assumed to be filled with w_1. Then *nw*, w_2, *nw*, and w_2 were sequentially injected into the system at a constant rate (0.05 m/s) for 0.15 s.

2.4. Quantification of Fluid Saturations

Based on the simulations mentioned in Section 2.3, all the computed results, including α_{w1}, α_{w2}, and α_{nw}, were recorded. To further investigate the displacement efficiency, the fluid saturations were quantified using the data extracted from the simulation results at each time step. The fluid saturations (S) were calculated as follows:

$$S_{w1} = \frac{\sum_{i=1}^{n} \alpha_{w1}}{\sum_{i=1}^{n} (\alpha_{w1} + \alpha_{w2} + \alpha_{nw})} \quad (6)$$

$$S_{w2} = \frac{\sum_{i=1}^{n} \alpha_{w2}}{\sum_{i=1}^{n} (\alpha_{w1} + \alpha_{w2} + \alpha_{nw})} \quad (7)$$

$$S_{nw} = \frac{\sum_{i=1}^{n} \alpha_{nw}}{\sum_{i=1}^{n} (\alpha_{w1} + \alpha_{w2} + \alpha_{nw})} \quad (8)$$

where n was the total number of cells in the simulation. All the saturation data, including S_{w1}, S_{w2}, and S_{nw}, mentioned in this study were quantified using the central area (the quadrilateral region was formed by the four centers of circles in four corners, such as the yellow quadrilateral in Figure 1). In addition, the normalized concentration (C/C_0) represented in Figure 2 was defined as the following equation:

$$\frac{C}{C_0} = \frac{\sum_{i=1}^{n} (\alpha_{w1})_{t=i}}{\sum_{i=1}^{n} (\alpha_{w1})_{t=0}} \quad (9)$$

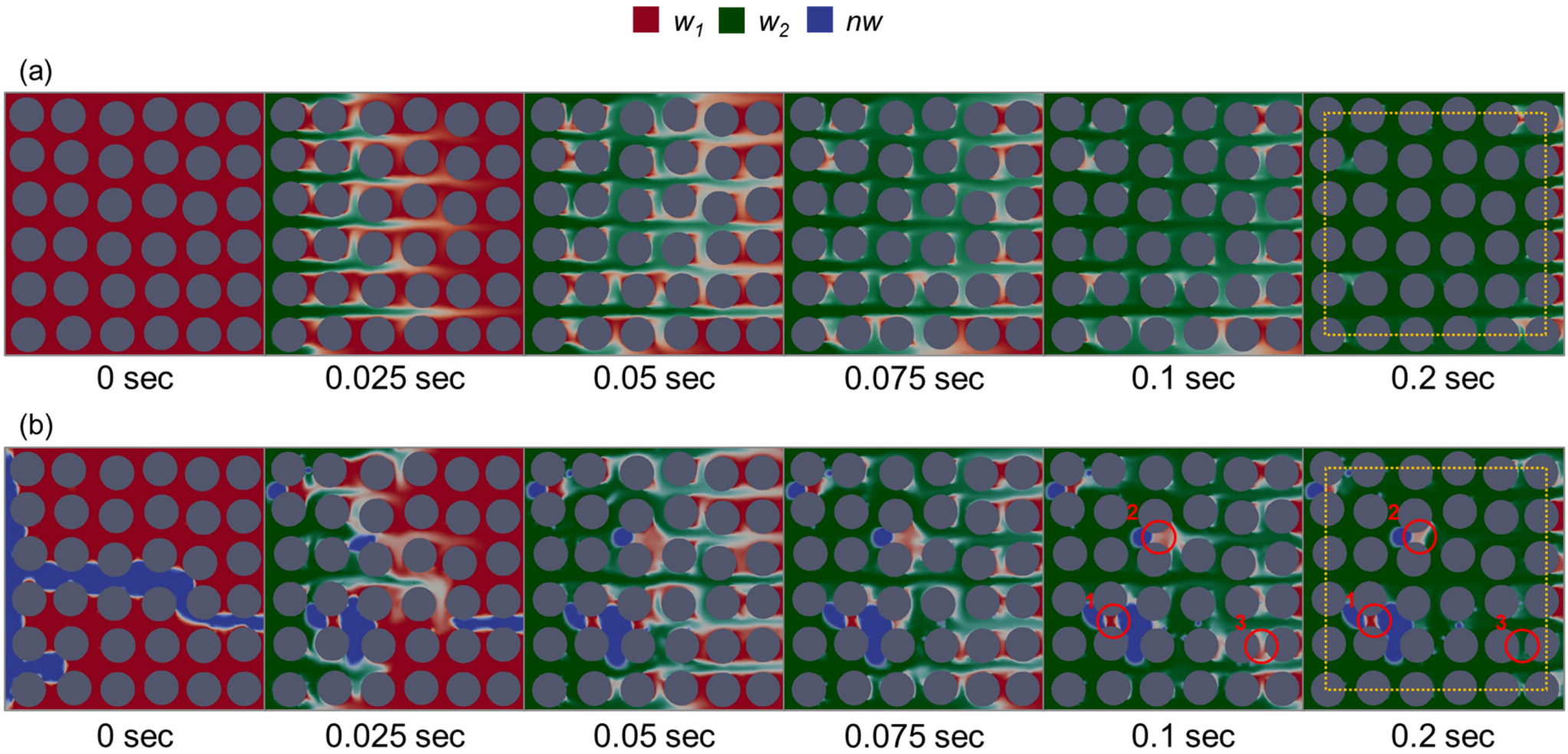

Figure 1. The displacement processes of w_1 by w_2 at a constant rate (0.05 m/s) in porous media (Micromodel 1) (**a**) without *nw*; (**b**) with *nw*. Red circle 1 in subfigure (**b**) is the region where w_1 was trapped by *nw*. Red circle 2 in subfigure (**b**) is the region where *nw* hindered the mixing of w_1 and w_2. Red circle 3 in subfigure (**b**) is the region where w_1 was displaced without being affected by *nw*.

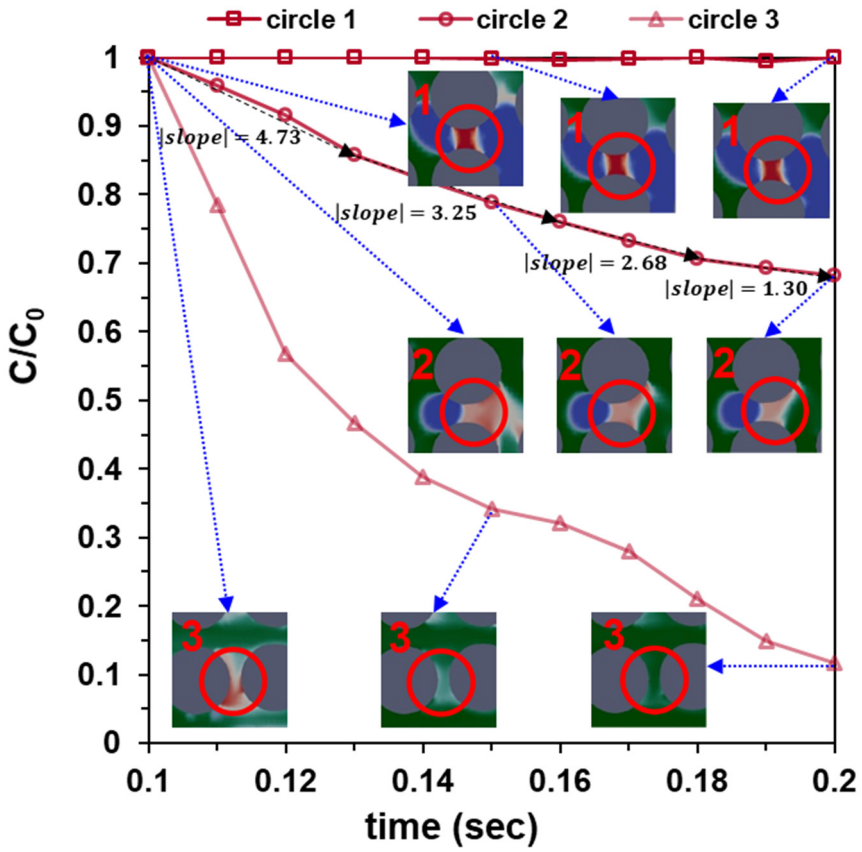

Figure 2. The normalized concentration (C/C_0) of w_1 in Figure 1b red circle regions versus time.

3. Results and Discussions

3.1. Effect of the Non-Wetting Phase (nw)

Figure 1 compares the displacement processes of w_1 by w_2 in porous media under the condition without *nw* to the condition with *nw*. From Figure 1a, it can be observed that w_1 in the porous system (Micromodel 1) without *nw* gradually mixed with w_2 and was displaced. On the other hand, Figure 1b shows that when *nw* existed in the porous system, *nw* would hinder the displacement of w_1. Even though *nw* was partially flushed out of the system, *nw* remained in the system and hindered the displacement of w_1 either by trapping it, such as the red circle 1 region in Figure 1b (C/C_0 remained constant in Figure 2), or by limiting the interaction of w_2 with w_1, such as in Figure 1b shown by the red circle 2 region. In the red circle 1 region, w_1 was trapped by *nw* and could not contact w_2. In the red circle 2 region, *nw* occupied the main flow path of the displacement, thus impeding the mixing of w_1 and w_2. This result indicated that the remaining *nw* in the porous system would affect the displacement of w_1 by w_2.

Ideally, w_1 should be totally displaced by w_2 after a long period of flushing. However, based on the column experiments implemented by Gouet-Kaplan et al. (2012) [13], the old water was still released from the unsaturated porous media over a long period of flushing by the new water. The phenomenon can be interpreted from pore scale observation and quantification based on simulation results in this study. Figure 2 shows the normalized concentration (C/C_0) of w_1 in Figure 1b red circle regions versus time. In Figure 2, the time span was from t = 0.1 s to t = 0.2 s in Figure 1b, where t = 0.1 s represented the start of monitoring and t = 0.2 s represented the end of monitoring. In the red circle 1 region, C/C_0 remained constant, which meant that w_1 was totally trapped by *nw*. In the red circle 2 region, C/C_0 decreased to 85.8% ($|\text{slope}| = 4.73$) from t = 0.1 s to t = 0.13 s, decreased to 76.0% ($|\text{slope}| = 3.25$) from t = 0.13 s to t = 0.16 s, decreased to 70.7% ($|\text{slope}| = 2.68$) from t = 0.16 s to t = 0.18 s, and decreased to 68.1% ($|\text{slope}| = 1.30$) from t = 0.18 s to

t = 0.2 s. The more and more slow decrease in C/C_0 implied that w_1 would be continuously released even after a long period of flushing. In the red circle 3 region, C/C_0 significantly decreased to 34.2% from t = 0.1 s to t = 0.15 s and continuously decreased to 11.8% from t = 0.15 s to t = 0.2 s. This indicated that w_1 would be gradually displaced without the interference of *nw*. The results of Figure 2 illustrated that when *nw* occupied the main path for displacement, w_1 nearby *nw* would not be easily displaced completely and only be partially released very slowly.

Although not all the remaining *nw* in porous media hindered the displacement of w_1, more *nw* pockets indicated more opportunity to cause the phenomenon of slow release of w_1 mentioned above. Table 2 summarizes the displacement results of all six micromodels under the conditions with *nw*. Micromodel 1, Micromodel 2, and Micromodel 3 (the three micromodels were slightly different in the grain distribution) had different remaining *nw* pockets and distributions, which resulted in very different displacement and mixing of w_1. The slight differences in geometry could result in significant displacement results when *nw* is involved.

Theoretically, the capillary pressure increases with decreasing the pore throat size (Young–Laplace equation $p_c = \frac{2\sigma cos\theta}{r}$, where p_c is the capillary pressure, r is the mean curvature, σ is the interfacial tension, and θ is the contact angle). Therefore, the snap-off phenomenon occurs more easily in porous media with narrower pore channels due to the larger interfacial instability between two immiscible fluids, leading to more *nw* pockets trapped in the pores. For the micromodels (Micromodel 1, Micromodel 4, and Micromodel 5) with similar porosity and different average pore throats, the number of remaining *nw* pockets increased with decreasing the average pore throat. Micromodel 4, with the smallest average pore throat (1.66×10^{-4} m), had the maximum number of the remaining *nw* pockets, which implied that it was the most difficult to completely displace w_1 in Micromodel 4. As for Micromodel 6, whose porosity (65.09%) is much larger than the other five micromodels (49.73% or 48.39%), the number of the remaining *nw* pockets was basically smaller than others, except Micromodel 5.

Table 2. Summary of the displacement results under the condition with *nw*.

Micromodel	Porosity (%)	Average Pore Radius (m)	Average Pore Throat (m)	Number of the Remaining *nw* Pockets	Final Image
Micromodel 1	49.73	3.53×10^{-4}	2.39×10^{-4}	4	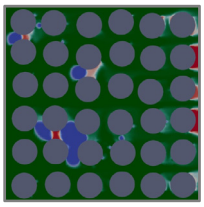
Micromodel 2	49.73	3.53×10^{-4}	2.36×10^{-4}	3	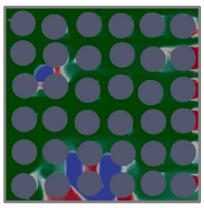
Micromodel 3	49.73	3.53×10^{-4}	2.38×10^{-4}	6	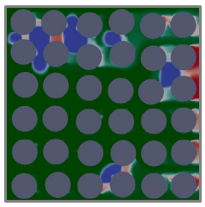

Table 2. *Cont.*

Micromodel	Porosity (%)	Average Pore Radius (m)	Average Pore Throat (m)	Number of the Remaining *nw* Pockets	Final Image
Micromodel 4	48.39	2.63×10^{-4}	1.66×10^{-4}	12	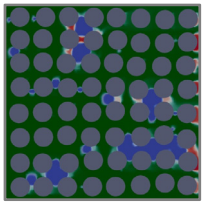
Micromodel 5	49.73	4.41×10^{-4}	2.73×10^{-4}	1	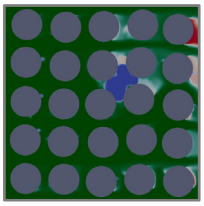
Micromodel 6	65.09	5.24×10^{-4}	4.37×10^{-4}	3	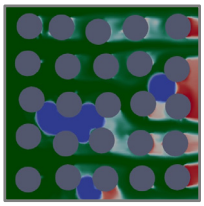

3.2. Effects of Interfacial Tension (σ_{w1nw}) and Contact Angle (θ)

Figure 3 shows fluid saturations versus time during displacement with different interfacial tensions (σ_{w1nw}) between w_1 and nw and images of displacement results at t = 0.2 s. All the properties of fluids for simulation were the same as in Table 1 and σ_{w1nw} decreased to half of the original value for comparison when w_2 started entering the system. When the properties listed in Table 1 were applied to the simulations of Micromodel 1, Micromodel 2, and Micromodel 3, in which w_1 and w_2 have the same density (ρ), viscosity (ν), and interfacial tension (σ), the S_{w1} of Micromodel 1, Micromodel 2, and Micromodel 3 were 4.30%, 6.67%, and 6.85% at t = 0.2 s, respectively. All three cases had a similar phenomenon in that some w_1 were trapped by nw and some nw occupied the main flow paths, resulting in the incomplete mixing zones of w_1 and w_2 (Figure 3b,e,h).

When σ_{w1nw} decreased to 0.03535 kg/s^2 (half of the original value), S_{w1} of Micromodel 1 and Micromodel 2 decreased to 1.88% and 2.48% at t = 0.2 s, but that of Micromodel 3 increased to 9.10%, even higher than the original simulation result (6.85%). Based on Figure 3c,f,i, it could be found that, unlike the original simulation results, most of nw were flushed out and could not interfere with the displacements of w_1. However, when nw remained in the system, the displacement of w_1 was still significantly hindered by nw.

Figure 4 showed fluid saturations versus time during displacement with different contact angles (θ) and images of displacement results at t = 0.2 s. All the properties of fluids for simulation were the same as in Table 1 and θ decreased from 45° to 30° for comparison when w_2 started entering the system. Figure 4a,d,g shows that when the contact angle (θ) was adjusted from 45° to 30°, the displacement results were different with no rules. For Micromodel 1, S_{nw} slightly increased from 7.13% to 9.67%, but S_{w1} dramatically increased from 4.30% to 16.24%. For Micromodel 2, S_{nw} decreased from 7.42% to 5.32%, and S_{w1} decreased from 6.67% to 5.34%. For Micromodel 3, S_{nw} increased from 11.95% to 12.17%, and S_{w1} increased from 6.85% to 8.35%. Based on Figure 4b,c,e,f,h,i, it could be found that a change in the contact angle (θ) affected the distribution of the remaining nw in the porous

system. This result implied that the contact angle (θ) influenced the immiscible fluids flow pattern, thus causing a different displacement efficiency of w_1.

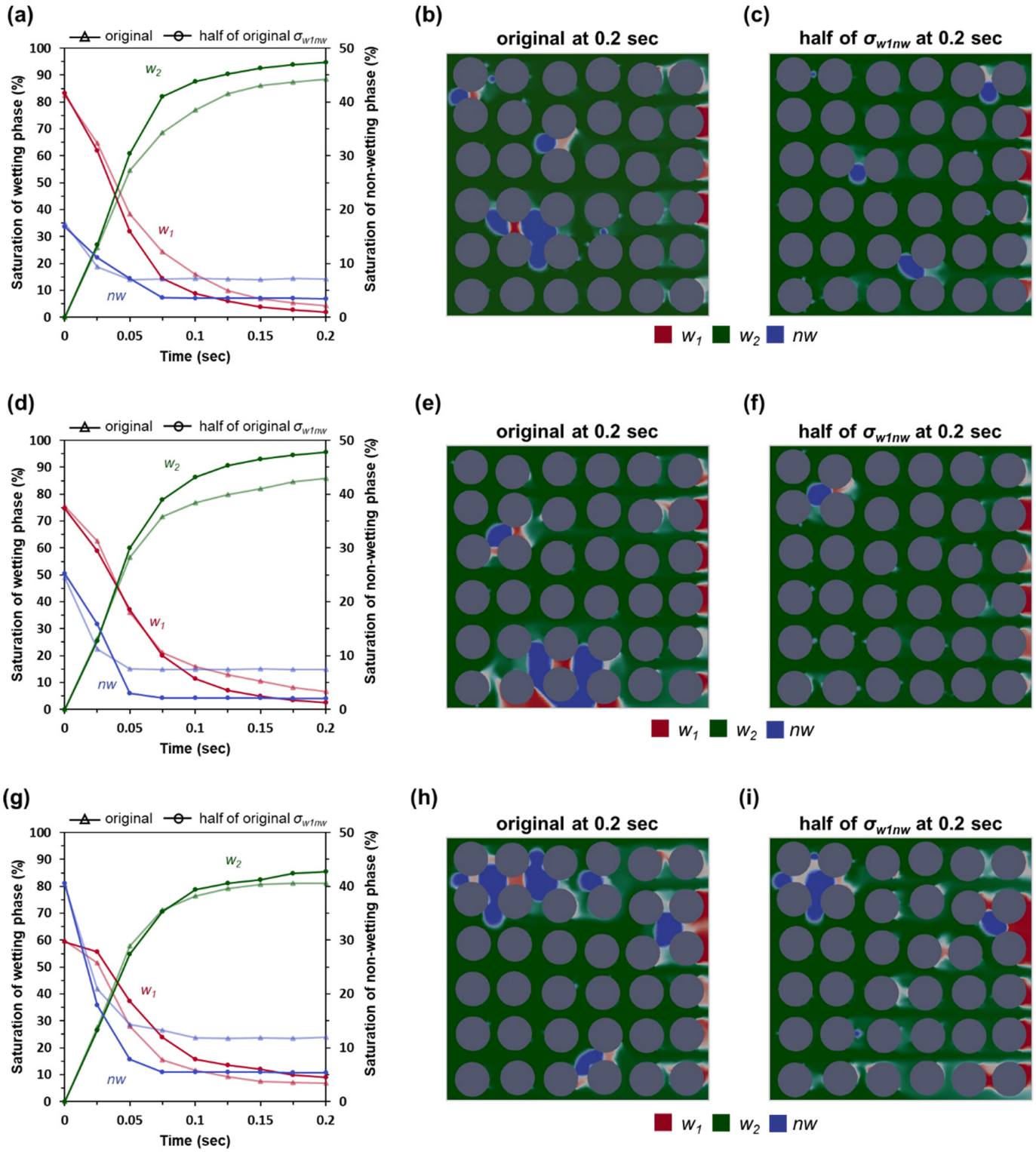

Figure 3. Effect of interfacial tension (σ_{w1nw}) on the displacement of w_1 in porous media with nw. (**a**–**c**) Micromodel 1; (**d**–**f**) Micromodel 2; (**g**–**i**) Micromodel 3.

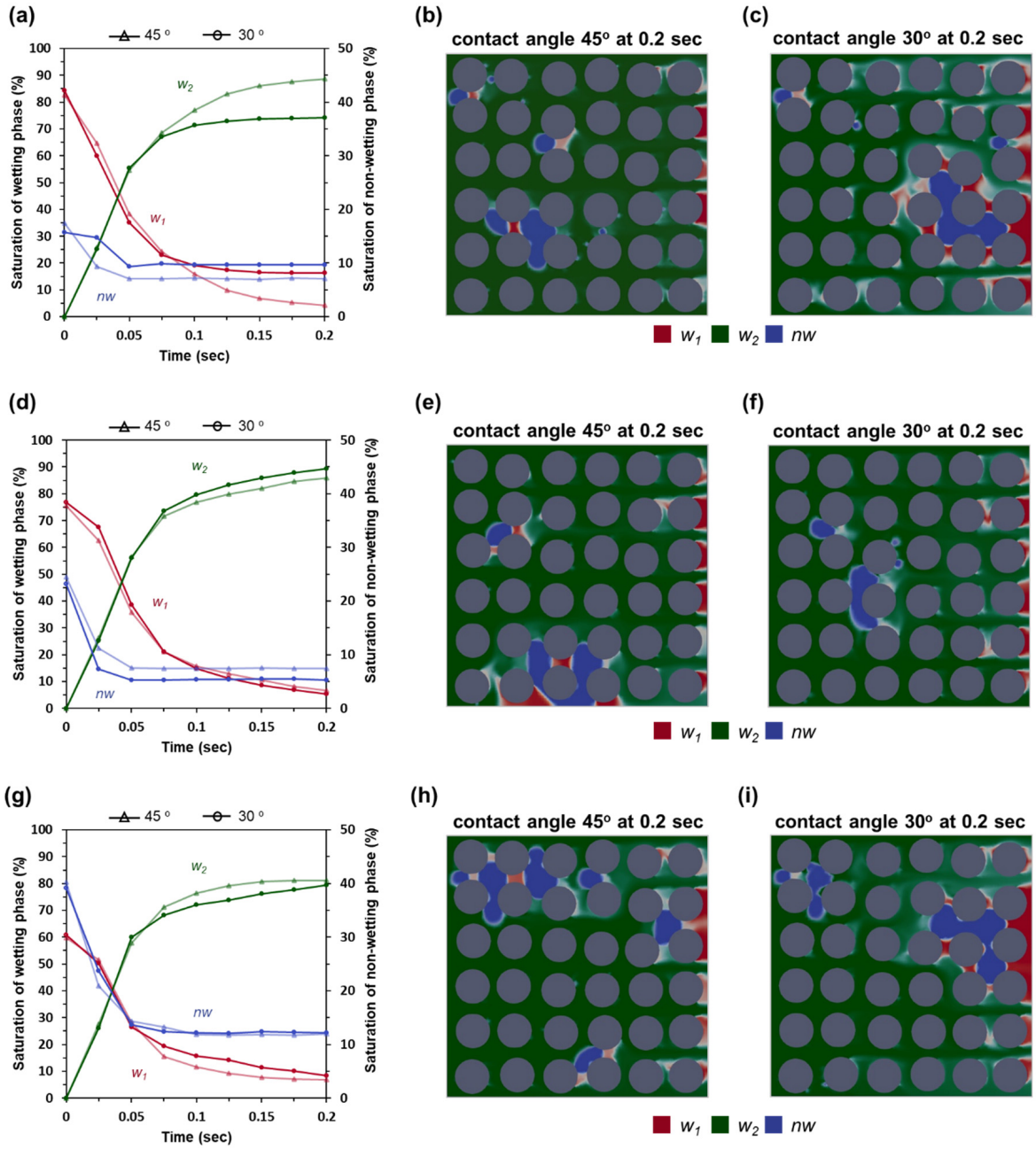

Figure 4. Effect of contact angle (θ) on the displacement of w_1 in porous media with *nw*. (**a**–**c**) Micromodel 1; (**d**–**f**) Micromodel 2; (**g**–**i**) Micromodel 3.

3.3. Effect of Injection Rate

Figure 5 shows fluid saturations under different injection rate conditions (Figure 5a) and images of displacement results (Figure 5b,c). All the properties of fluids for simulation were the same as in Table 1. Based on Figure 5a, it could be found that S_{nw} under a low injection rate condition (0.01 m/s) is much larger than under a high injection rate condition (0.05 m/s) because a lower driving force (Capillary number $C_a = 1.41 \times 10^{-4}$) could not effectively flush out *nw*. In addition, w_1 was not efficiently displaced by w_2 under low injection rate conditions. This result implied that low injection rates might cause more of *nw* to remain in the porous medium, which could hinder the displacement of w_1.

Figure 5c shows that although w_2 displaced w_1 through contact areas, *nw* did block some routes (longitudinal direction) and prevent w_2 from mixing with w_1. When there was more *nw* remaining in the porous medium, the displacement of w_1 was easier interfered

with by the remaining *nw*. This result demonstrated that a very low injection rate (0.01 m/s) could not effectively displace w_1 by w_2 in porous media with *nw*.

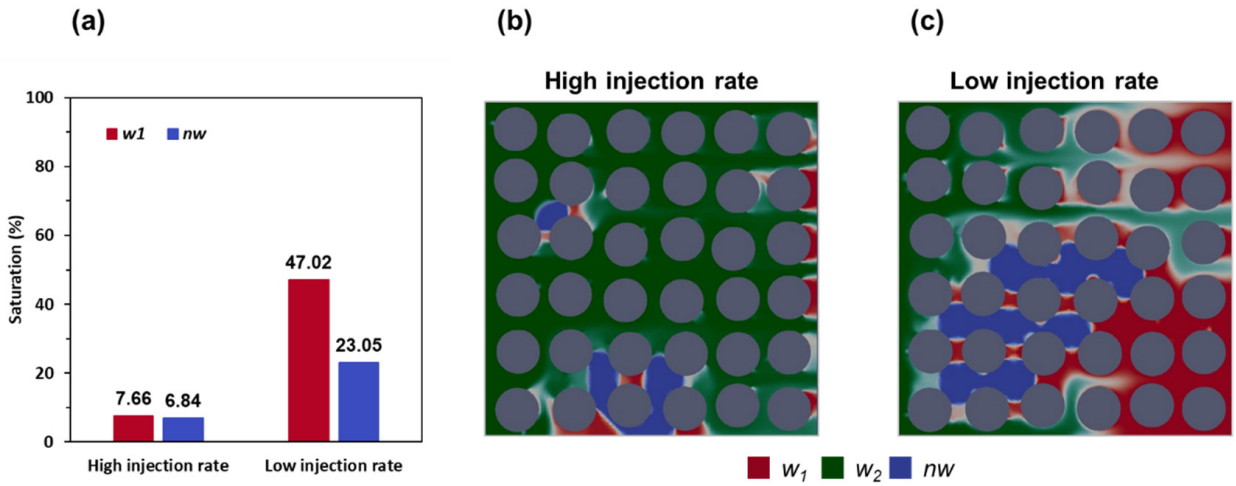

Figure 5. Effect of injection rate on the displacement of w_1 in the porous medium (Micromodel 2) with *nw*. w_2 entered the system at 0.05 m/s for 0.2 s for the high injection rate condition and at 0.01 m/s for 1 s for the low injection rate condition. (**a**) Fluid saturations; (**b**,**c**) images of displacement results.

3.4. Effect of Drainage–Imbibition Cycles

Figure 6 shows the fluid saturations after drainage–imbibition cycles. All the properties of fluids for simulation were the same as in Table 1. Initially, the system was assumed to be filled with w_1, and then two cycles of *nw* followed by w_2 were injected into the system. Based on Figure 6, it could be significantly observed that the S_{w1} was lower after the second cycle than after the first cycle in all six micromodels (one cycle represented one drainage–imbibition process). This result inferred that the drainage–imbibition cycles could improve the displacement of w_1. For instance, the S_{w1} decreased from 6.84% (first cycle) to 1.46% (second cycle) in Micromodel 1. However, it could be observed that the S_{nw}, the crucial factor affecting the displacement of w_1, decreased in Micromodel 3 (from 11.80% to 7.45%), Micromodel 4 (from 15.60% to 13.42%), and Micromodel 6 (from 13.26% to 10.57%), but increased in Micromodel 1 (from 7.01% to 12.03%), Micromodel 2 (from 7.51% to 14.28%), and Micromodel 5 (from 5.54% to 9.50%).

From Figure 6, it could be found that the distributions of *nw* after the first cycle were different from those after the second cycle. Some of w_1 originally trapped or limited by *nw* after the first cycle re-contacted w_2 and were displaced by them during the second cycle. Micromodel 1, Micromodel 2, and Micromodel 3 had the same porosity and similar average pore throats. Although the hindrance patterns of *nw* on the displacement of Micromodel 1, Micromodel 2, and Micromodel 3 were different, causing significantly different S_{w1} after the first cycle, when the regions where *nw* hindered the displacements of w_1 were broken during the second cycle process, the S_{w1} of the three micromodels were similar after the second cycle (Figure 6a–c).

However, not all the regions where *nw* hindered the displacements of w_1 formed during the first cycle would be broken during the second cycle. In Micromodel 4, the one originally with the maximum number of the remaining *nw* pockets due to its smallest average pore throat, the region where w_1 was trapped by *nw* (the upper middle area of the micromodel) still existed after the second cycle (Figure 6d). Even in a micromodel with a larger average pore throat, it did not mean that *nw*, which hindered the displacement, would be absolutely removed. In Micromodel 5, the one with similar porosity to Micromodel 1 and Micromodel 4 but with a larger average pore throat, the slightly upper right area in the middle of the micromodel continuously affected the displacement of w_1 after the second cycle (Figure 6e) although the S_{w1} significantly decreased during the second cycle process.

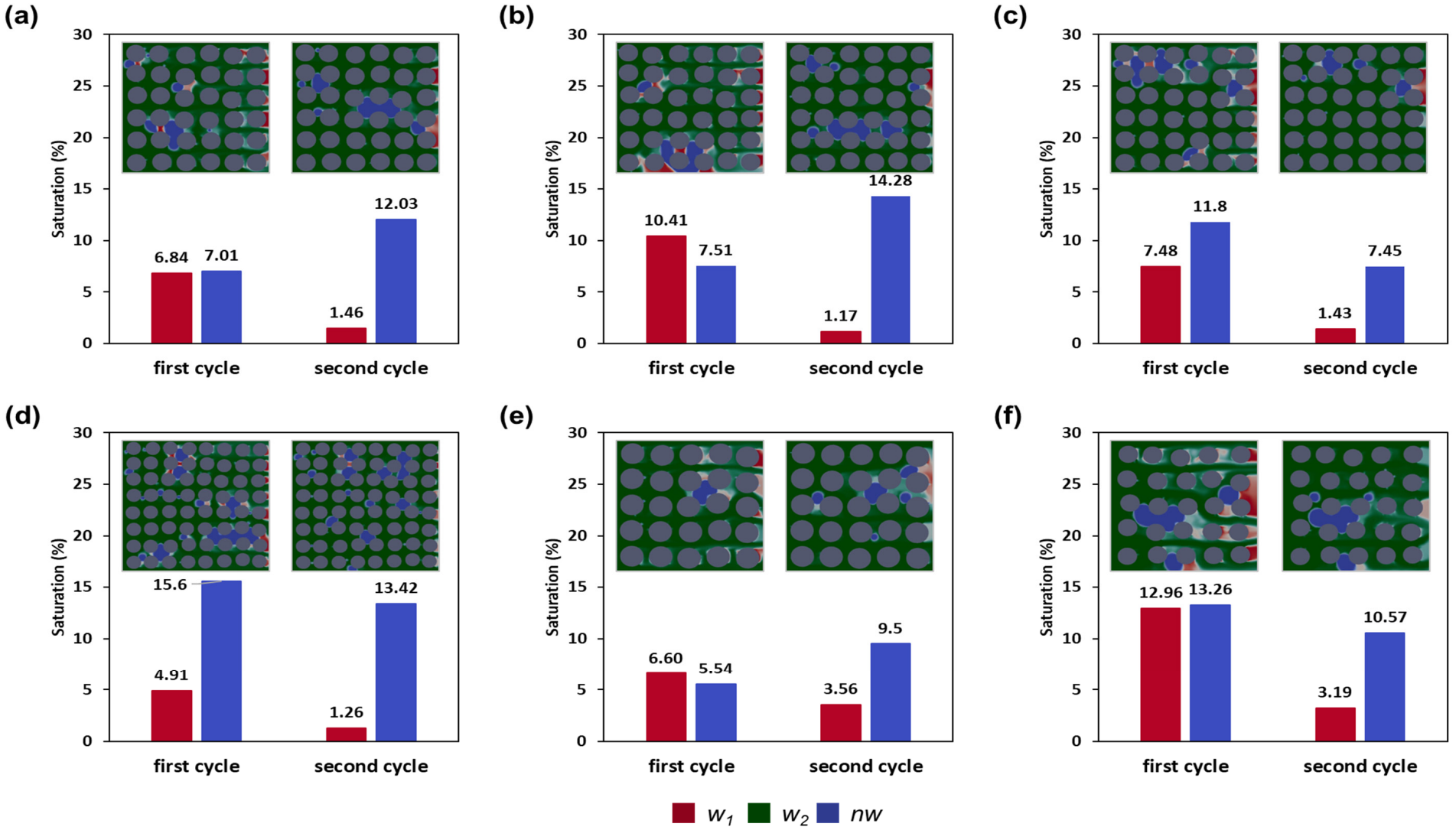

Figure 6. Effect of drainage–imbibition cycles on the displacement of w_1 in porous media. (**a**) Micromodel 1; (**b**) Micromodel 2; (**c**) Micromodel 3; (**d**) Micromodel 4; (**e**) Micromodel 5; (**f**) Micromodel 6.

In Micromodel 6, the one with the largest porosity of all six micromodels, the S_{w1} decreased from 12.96% (first cycle) to 3.19% (second cycle). The decrease in S_{w1} was more obvious than those of other micromodels with lower porosity. This was because when one *nw* pocket, which originally hindered the displacement of w_1 after the first cycle, was removed after the second cycle, a large amount of w_1 was rapidly displaced by w_2. This result implied that the effect of the drainage–imbibition cycle on the displacement of w_1 was more significant in micromodels with larger porosity.

3.5. Environmental Significance

Based on the above simulation results, we evaluated the factors affecting the displacement of w_1 by w_2 in the porous media and successfully investigated the potential mechanism. Furthermore, these simulation findings not only provided new directions for academic research but also contributed to a more comprehensive perspective and a deeper understanding of engineering applications.

In Section 3.1, it was demonstrated that the phenomena observed in Darcy-scale experiments or field experiments can be explained through pore-scale simulations without being limited by traditional experimental designs or quantitative techniques. For instance, this study utilized pore-scale simulation results to elucidate the "slow-release phenomenon of old water" observed in previous column experiments.

In Section 3.2, we gained a more comprehensive understanding of the removal of pollutants in the unsaturated zone. For instance, the surface tension of perfluorooctanesulfonic acid (PFOS), a type of PFAS, varies with its concentration [7], which could lead to significant variations in displacement efficiency, even under the same spatial distribution conditions. Moreover, as the water evaporated, the pollutants dissolved in the resident water within the porous system would change in concentration, thereby altering the surface tension of the solution and further affecting the displacement.

In Section 3.3, we learned that in contrast to what was presented in the literature [26], a high injection rate did not necessarily result in a lower opportunity for the interaction between new and old water due to preferential flow. In this study, a high injection rate may lead to significant displacement efficiency as it facilitated the effective flushing out of the non-wetting fluid.

In Section 3.4, we understood that the drainage–imbibition cycles facilitated the displacement of w_1. Since this cycle occurs repetitively naturally in the environment, this finding carries not only theoretical implications but also practical significance in guiding future soil remediation strategies.

In the porous system's simulation, the capillary action of the wetting fluid was quite crucial because of the narrow pore channels, causing a significant pressure difference across the interface between two immiscible fluids. In SPH, the surface tension was not prescribed explicitly but was set by adding assumed forces between different particles [21]. Similar to SPH, the surface tension was modeled by using special forces between the lattice nodes in LBM [26,28]. With the advantage of DNS, parameters for simulation being the physical properties of the fluids, the computational method used in this study could authentically simulate other immiscible fluid–fluid flows in porous media. Combined with three-dimensional (3D) imaging techniques [35], which could reconstruct real porous structures, this method could easily predict the flow patterns in natural porous systems under different conditions by adjusting the physical properties (simulation parameters) without lab or field experiments.

4. Conclusions

This study simulated the displacement of w_1 by w_2 in porous media using DNS. A series of displacement simulations were carried out under different conditions. Using observation and quantification based on simulation results, the main conclusions can be summarized as follows:

(1) When nw existed in the porous system, the displacement of w_1 by w_2 would be impeded. By calculating (C/C_0) of w_1 in the regions hindered by nw, it could be observed that w_1 was displaced very slowly. This result helped explain the "slow-release phenomenon of old water" in previous column experiments.
(2) When σ_{w1nw} decreased to half of the original value, the S_{w1} would decrease because most of nw was flushed out. A change in contact angle (θ) caused a different distribution of nw in the system, which could result in a different displacement efficiency of w_1.
(3) At a very low injection rate = 0.01 m/s, w_2 could not effectively displace w_1 in porous media because of the remaining nw.
(4) The drainage–imbibition cycles could improve the displacement of w_1 in porous media because the constrained regions caused by nw were broken during consecutive drainage–imbibition cycles.
(5) The simulation results have significantly advanced our understanding of future research and applications. In addition, the DNS method authentically described the immiscible fluid–fluid flow in porous media and could be easily applied to study physical mechanisms in other natural or industrial systems.

Author Contributions: Conceptualization, Y.-L.W.; methodology, Y.-L.W.; software, validation, Y.-L.W.; formal analysis, Y.-L.W.; investigation, Y.-L.W.; data curation, Y.-L.W.; writing—original draft, Y.-L.W.; visualization, Y.-L.W.; writing—review and editing, Q.-Z.H. and S.-Y.H.; resources, S.-Y.H.; supervision, S.-Y.H.; project administration, S.-Y.H.; funding acquisition, S.-Y.H. All authors have read and agreed to the published version of the manuscript.

Funding: This research was funded by the National Science and Technology Council, Taiwan under grant NSTC 111-2116-M-002-025.

Data Availability Statement: The data are available from the authors upon reasonable request.

Acknowledgments: The English editing of this article was sponsored by National Taiwan University with the support of the Higher Education Sprout Project from the Ministry of Education, Taiwan.

Conflicts of Interest: The authors declare no conflict of interest.

Appendix A

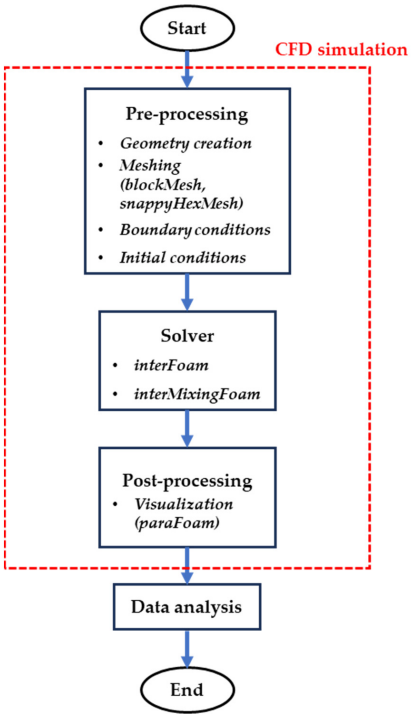

Figure A1. The workflow diagram of OpenFOAM software.

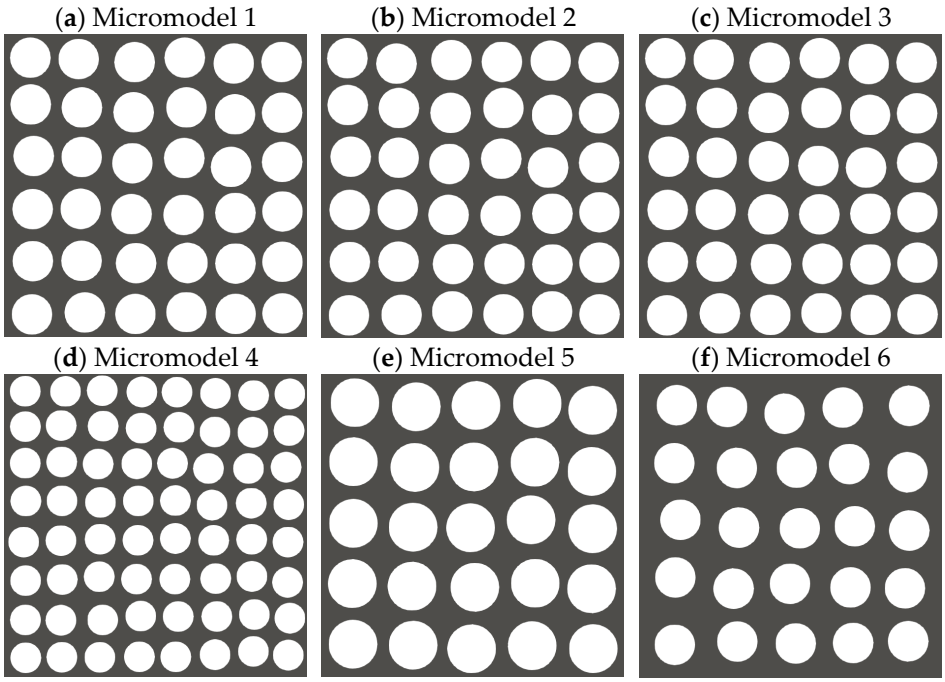

Figure A2. Diagrams of micromodels used in this study.

References

1. Kim, K.Y.; Oh, J.; Han, W.S.; Park, K.G.; Shinn, Y.J.; Park, E. Two-phase flow visualization under reservoir conditions for highly heterogeneous conglomerate rock: A core-scale study for geologic carbon storage. *Sci. Rep.* **2018**, *8*, 4869. [CrossRef] [PubMed]
2. Seyedpour, S.M.; Thom, A.; Ricken, T. Simulation of Contaminant Transport through the Vadose Zone: A Continuum Mechanical Approach within the Framework of the Extended Theory of Porous Media (eTPM). *Water* **2023**, *15*, 343. [CrossRef]
3. Wang, L.; He, Y.; Wang, Q.; Liu, M.; Jin, X. Multiphase flow characteristics and EOR mechanism of immiscible CO_2 water-alternating-gas injection after continuous CO_2 injection: A micro-scale visual investigation. *Fuel* **2020**, *282*, 118689. [CrossRef]
4. Wang, Y.; Fernàndez-Garcia, D.; Sole-Mari, G.; Rodríguez-Escales, P. Enhanced NAPL Removal and Mixing with Engineered Injection and Extraction. *Water Resour. Res.* **2022**, *58*, e2021WR031114. [CrossRef]
5. Per- and Polyfluoroalkyl Substances (PFAS). Available online: https://www.epa.gov/pfas (accessed on 1 June 2023).
6. Abraham, J.E.F.; Mumford, K.G.; Patch, D.J.; Weber, K.P. Retention of PFOS and PFOA Mixtures by Trapped Gas Bubbles in Porous Media. *Environ. Sci. Technol.* **2022**, *56*, 15489–15498. [CrossRef]
7. Guo, B.; Zeng, J.; Brusseau, M.L. A Mathematical Model for the Release, Transport, and Retention of Per- and Polyfluoroalkyl Substances (PFAS) in the Vadose Zone. *Water Resour. Res.* **2020**, *56*, e2019WR026667. [CrossRef]
8. Ji, Y.; Yan, N.; Brusseau, M.L.; Guo, B.; Zheng, X.; Dai, M.; Liu, H.; Li, X. Impact of a Hydrocarbon Surfactant on the Retention and Transport of Perfluorooctanoic Acid in Saturated and Unsaturated Porous Media. *Environ. Sci. Technol.* **2021**, *55*, 10480–10490. [CrossRef]
9. Wang, Y.; Khan, N.; Huang, D.; Carroll, K.C.; Brusseau, M.L. Transport of PFOS in aquifer sediment: Transport behavior and a distributed-sorption model. *Sci. Total Environ.* **2021**, *779*, 146444. [CrossRef]
10. Wang, Z.; Feyen, J.; van Genuchten, M.T.; Nielsen, D.R. Air entrapment effects on infiltration rate and flow instability. *Water Resour. Res.* **1998**, *34*, 213–222. [CrossRef]
11. Wei, Y.; Chen, K.; Wu, J. Estimation of the Critical Infiltration Rate for Air Compression During Infiltration. *Water Resour. Res.* **2020**, *56*, e2019WR026410. [CrossRef]
12. Gouet-Kaplan, M.; Berkowitz, B. Measurements of Interactions between Resident and Infiltrating Water in a Lattice Micromodel. *Vadose Zone J.* **2011**, *10*, 624–633. [CrossRef]
13. Gouet-Kaplan, M.; Arye, G.; Berkowitz, B. Interplay between resident and infiltrating water: Estimates from transient water flow and solute transport. *J. Hydrol.* **2012**, *458–459*, 40–50. [CrossRef]
14. Si, L.; Xi, Y.; Wei, J.; Wang, H.; Zhang, H.; Xu, G.; Liu, Y. The influence of inorganic salt on coal-water wetting angle and its mechanism on eliminating water blocking effect. *J. Nat. Gas. Sci. Eng.* **2022**, *103*, 104618. [CrossRef]
15. Henry, E.J.; Smith, J.E. The effect of surface-active solutes on water flow and contaminant transport in variably saturated porous media with capillary fringe effects. *J. Contam. Hydrol.* **2002**, *56*, 247–270. [CrossRef]
16. Li, Y.; Flores, G.; Xu, J.; Yue, W.Z.; Wang, Y.X.; Luan, T.G.; Gu, Q.B. Residual air saturation changes during consecutive drainage-imbibition cycles in an air-water fine sandy medium. *J. Hydrol.* **2013**, *503*, 77–88. [CrossRef]

17. Tavangarrad, A.H.; Hassanizadeh, S.M.; Rosati, R.; Digirolamo, L.; van Genuchten, M.T. Capillary pressure–saturation curves of thin hydrophilic fibrous layers: Effects of overburden pressure, number of layers, and multiple imbibition–drainage cycles. *Text. Res. J.* **2019**, *89*, 4906–4915. [CrossRef]
18. Gramling, C.M.; Harvey, C.F.; Meigs, L.C. Reactive Transport in Porous Media: A Comparison of Model Prediction with Laboratory Visualization. *Environ. Sci. Technol.* **2002**, *36*, 2508–2514. [CrossRef]
19. Oates, P.M.; Harvey, C.F. A colorimetric reaction to quantify fluid mixing. *Exp. Fluids.* **2006**, *41*, 673–683. [CrossRef]
20. De Anna, P.; Jimenez-Martinez, J.; Tabuteau, H.; Turuban, R.; Le Borgne, T.; Derrien, M.; Méheust, Y. Mixing and Reaction Kinetics in Porous Media: An Experimental Pore Scale Quantification. *Environ. Sci. Technol.* **2014**, *48*, 508–516. [CrossRef]
21. Gouet-Kaplan, M.; Tartakovsky, A.; Berkowitz, B. Simulation of the interplay between resident and infiltrating water in partially saturated porous media. *Water Resour. Res.* **2009**, *45*, W05416. [CrossRef]
22. Bandara, U.C.; Tartakovsky, A.M.; Palmer, B.J. Pore-scale study of capillary trapping mechanism during CO_2 injection in geological formations. *Int. J. Greenh. Gas. Control* **2011**, *5*, 1566–1577. [CrossRef]
23. Bandara, U.C.; Tartakovsky, A.M.; Oostrom, M.; Palmer, B.J.; Grate, J.; Zhang, C. Smoothed particle hydrodynamics pore-scale simulations of unstable immiscible flow in porous media. *Adv. Water Resour.* **2013**, *62*, 356–369. [CrossRef]
24. Baakeem, S.S.; Bawazeer, S.A.; Mohamad, A.A. Comparison and evaluation of Shan–Chen model and most commonly used equations of state in multiphase lattice Boltzmann method. *Int. J. Multiph. Flow.* **2020**, *128*, 103290. [CrossRef]
25. Li, P.; Berkowitz, B. Characterization of mixing and reaction between chemical species during cycles of drainage and imbibition in porous media. *Adv. Water Resour.* **2019**, *130*, 113–128. [CrossRef]
26. Li, P.; Berkowitz, B. Controls on interactions between resident and infiltrating waters in porous media. *Adv. Water Resour.* **2018**, *121*, 304–315. [CrossRef]
27. Ferrari, A.; Lunati, I. Direct numerical simulations of interface dynamics to link capillary pressure and total surface energy. *Adv. Water Resour.* **2013**, *57*, 19–31. [CrossRef]
28. Ferrari, A.; Jimenez-Martinez, J.; Le Borgne, T.; Méheust, Y.; Lunati, I. Challenges in modeling unstable two-phase flow experiments in porous micromodels. *Water Resour. Res.* **2015**, *51*, 1381–1400. [CrossRef]
29. Meakin, P.; Tartakovsky, A.M. Modeling and simulation of pore-scale multiphase fluid flow and reactive transport in fractured and porous media. *Rev. Geophys.* **2009**, *47*, RG3002. [CrossRef]
30. OpenFOAM v9. Available online: https://openfoam.org/version/9/ (accessed on 1 June 2023).
31. Hirt, C.W.; Nichols, B.D. Volume of fluid (VOF) method for the dynamics of free boundaries. *J. Comput. Phys.* **1981**, *39*, 201–225. [CrossRef]
32. Ambekar, A.S.; Mattey, P.; Buwa, V.V. Pore-resolved two-phase flow in a pseudo-3D porous medium: Measurements and volume-of-fluid simulations. *Chem. Eng. Sci.* **2021**, *230*, 116128. [CrossRef]
33. Aziz, R.; Joekar-Niasar, V.; Martinez-Ferrer, P. Pore-scale insights into transport and mixing in steady-state two-phase flow in porous media. *Int. J. Multiph. Flow.* **2018**, *109*, 51–62. [CrossRef]
34. Deshpande, S.S.; Anumolu, L.; Trujillo, M.F. Evaluating the performance of the two-phase flow solver interFoam. *Comput. Sci. Discov.* **2012**, *5*, 014016. [CrossRef]
35. Ziegler, A.; Bock, C.; Ketten, D.R.; Mair, R.W.; Mueller, S.; Nagelmann, N.; Pracht, E.D.; Schröder, L. Digital Three-Dimensional Imaging Techniques Provide New Analytical Pathways for Malacological Research. *Am. Malacol. Bull.* **2018**, *36*, 248–273. [CrossRef]

Disclaimer/Publisher's Note: The statements, opinions and data contained in all publications are solely those of the individual author(s) and contributor(s) and not of MDPI and/or the editor(s). MDPI and/or the editor(s) disclaim responsibility for any injury to people or property resulting from any ideas, methods, instructions or products referred to in the content.